

Advancing Reversible Magnesium–Sulfur Batteries with a Self-Standing Gel Polymer Electrolyte

Liping Wang,* Sibylle Riedel, Alexander Welle, Smobin Vincent, Sirshendu Dinda, Bosubabu Dasari, Juan Maria Garcia Lastra, Birgit Esser, and Zhirong Zhao-Karger



Cite This: *ACS Appl. Energy Mater.* 2024, 7, 5857–5868



Read Online

ACCESS |



Metrics & More



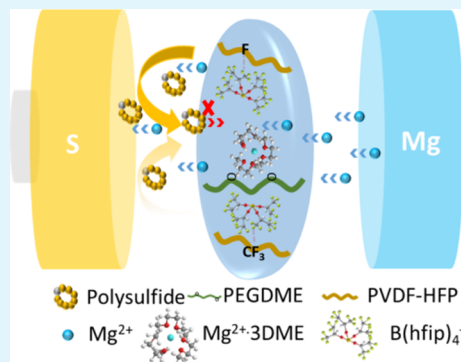
Article Recommendations



Supporting Information

ABSTRACT: Magnesium (Mg) metal batteries exhibit great potential as energy storage systems beyond lithium, owing to their inherent safety, material sustainability, and low cost. However, their development is hindered by the lack of a suitable electrolyte enabling a reversible Mg deposition and dissolution. When combined with a sulfur (S) cathode, the formation of magnesium polysulfide intermediates further restricts the cycling stability of sulfur-based batteries. In this study, a flexible Mg-based gel polymer electrolyte is designed to address these challenges in Mg metal batteries. Fabricated through a straightforward solvent-casting approach using magnesium tetrakis(hexafluoroisopropoxy)borate salt, the gel polymer electrolyte demonstrates positive interactions between the borate anion and polymer, facilitating efficient Mg-ion transfer. Remarkably, the gel polymer electrolyte exhibits reversible Mg plating/stripping over 1000 cycles and significantly enhanced cycling performance for up to 300 cycles when incorporated with a sulfur cathode. These findings highlight the potential of gel polymer electrolytes to enable reversible Mg deposition and dissolution, enhance the life span of Mg–S batteries, and advance the field of Mg metal batteries.

KEYWORDS: gel polymer electrolyte, reversible Mg deposition and dissolution, magnesium metal batteries, polysulfide shuttle, magnesium–sulfur batteries



INTRODUCTION

Rechargeable magnesium (Mg) batteries (RMBs) are considered to be one of the most promising candidates for post-lithium (Li) battery systems due to the high theoretical gravimetric and volumetric capacities (2205 mA h g⁻¹ and 3833 mA h mL⁻¹), as well as the high natural abundance and low cost of the Mg anode, particularly for large-scale battery production.^{1,2} Compared to Li, Mg has a high melting point (660 °C) and is environmentally friendly, which makes it easier and safer to handle during battery preparation.³ Additionally, except for some extreme conditions,⁴ the inherent nature of Mg to form a homogeneous surface during electrochemical plating diminishes the risk of dangerous dendrite growth, which is common for Li and regarded as a key issue impeding wider application of Li metal anodes in Li battery systems.^{5–8}

To take advantage of the benefits of the Mg anode, appropriate Mg-ion electrolytes are essential.^{9,10} Given the highly reductive nature of metal anodes, reactions between the components of organic electrolytes and Mg metal anodes cannot be avoided, resulting in the formation of an interfacial layer on the Mg metal surface. This layer may potentially passivate the anode surface and restrict the reversibility of Mg deposition.^{11–13} Some attempts have been made to address the unique interfacial issues by modifying the solid electrolyte interphases with optimized electrolyte components.^{14–17}

However, there is real need to enhance the range of available electrolytes for RMBs.

Apart from electrolyte, cathode materials that can provide high specific capacity are also required. With a double positive charge and an ionic radius of 0.72 Å, which is comparable to that of Li⁺ (0.76 Å), the Mg²⁺ ion has a much higher charge density, resulting in strong electrostatic interactions with the species in the electrolytes and active electrode materials.¹⁸ This characteristic hinders the diffusion of Mg ions into solid hosts, leading to slow solid-state diffusion kinetics in cathode structures, particularly for intercalation-type cathode materials. In this context, conversion-type cathode materials like sulfur (S) are highly promising candidates for RMBs. The volume increase during the conversion from S to MgS is approximately 28%, which is low when compared to other conversion-type cathode materials. Moreover, sulfur has a high theoretical specific capacity (1672 mA h g⁻¹ or 3459 mA h mL⁻¹), and the combination of a Mg anode with an S cathode can deliver a

Received: April 25, 2024

Revised: June 13, 2024

Accepted: June 13, 2024

Published: June 27, 2024



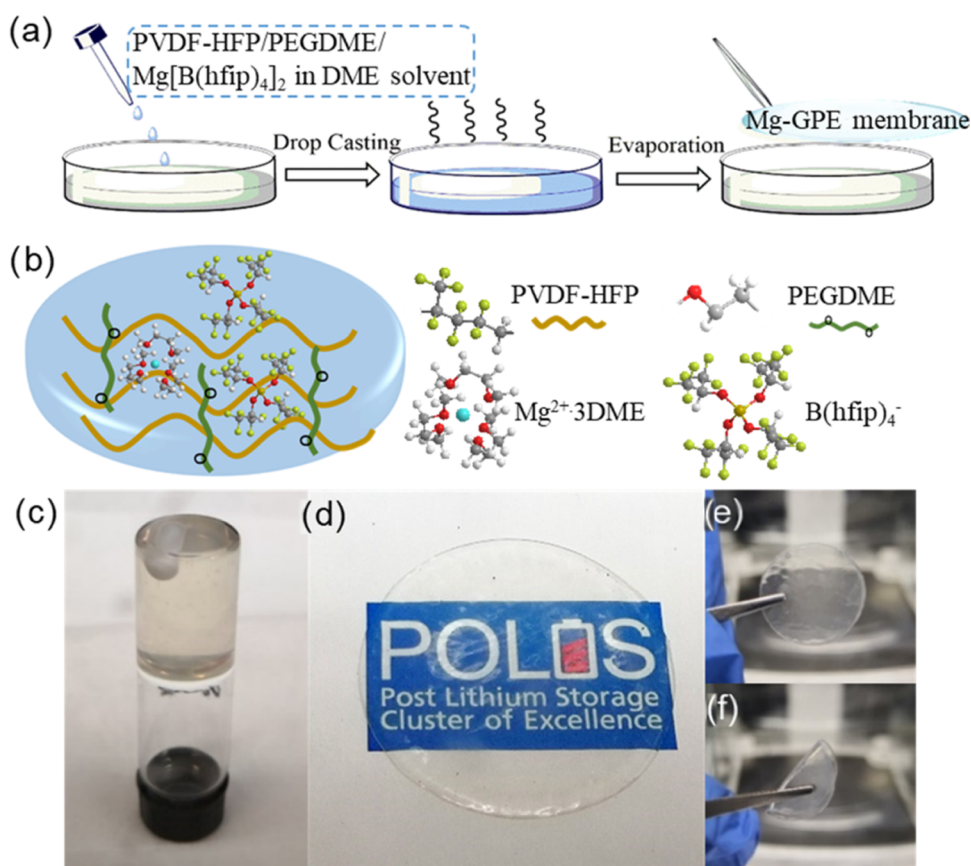


Figure 1. (a) Schematic illustration of the preparation of the Mg-GPE membrane. (b) Illustration of the composition of the Mg-GPE. Optical photographs of (c) the prepared gel solution kept overnight in the glovebox, (d) the pristine Mg-GPE membrane, and (e, f) the Mg-GPE disks cut into a specific size of 16 mm.

promising theoretical energy density of over 4000 Wh L⁻¹.^{19,20} Sulfur is also advantageous due to its low molecular weight, high natural abundance, and nontoxicity, making it a cost-effective option for energy storage systems. Despite the merits of combining an S cathode and a Mg anode, the development of Mg–S batteries is still in an early stage, which is restrained by the unavailability of suitable electrolytes that fulfill the specific requirements for Mg–S battery chemistry. An ideal electrolyte must be compatible with electrophilic sulfur and enable reversible Mg deposition simultaneously. Furthermore, due to the known “polysulfide shuttle” phenomenon of sulfur cathodes, Mg–S batteries are suffering from self-discharge, rapid capacity degradation, and poor cell life with liquid electrolytes.^{21,22}

To alleviate these problems, researchers have attempted various approaches to tune the electrolyte compositions, such as using electrolyte additives.^{23–25} However, the issue of active material dissolution in the liquid electrolytes remains a crucial challenge. A gel polymer electrolyte (GPE) with a low solvent content could be a rational option, offering an alternative approach for the development of future Mg–S battery systems. By retaining a small amount of organic solvents within a polymeric network, GPE can allow adequate Mg-ion mobility and at the same time limit the dissolution and diffusion of the soluble polysulfides. A similar concept has already been successfully employed in lithium–sulfur (Li–S) batteries.^{26,27} However, when it comes to Mg–S batteries, the elevated charge density of the Mg²⁺ ion inherently adds to the challenge of selecting suitable polymers, solvents, and Mg salts for GPEs.

To the best of our knowledge, there are only limited reports on GPEs designed for Mg–S batteries.^{28–30}

In this study, we employ the magnesium tetrakis (hexafluoroisopropoxy) borate Mg[B(hfip)₄]₂ (hfip = OCH(CF₃)₂) salt in combination with poly(vinylidene fluoride-*co*-hexafluoropropylene) (PVDF-HFP) and polyethylene glycol dimethyl ether (PEGDME) as a plasticizer to form a Mg-GPE. As a widely used polymer base for GPEs, PVDF-HFP features a good wettability in organic electrolytes and film-forming ability.³¹ By incorporating with the PEGDME plasticizer, which has a low viscosity, low volatility, and low flammability,³² a free-standing flexible electrolyte membrane can be obtained. This chloride (Cl)-free GPE is chemically compatible with various electrodes and battery components and allows for uniform Mg deposition with long-term cycling stability, making it an excellent alternative to the commonly used Cl-containing Mg electrolyte for RMBs. In addition, the Mg-GPE was employed in Mg–S cells and exhibited superior cycling stability, which was attributed to the suppression of the magnesium polysulfide shuttle with the gel electrolyte membrane. These findings demonstrate the promising attributes of GPEs for RMBs.

RESULTS AND DISCUSSION

Preparation and Characterization. The electrolyte membrane was prepared using a typical solvent-casting method, as illustrated in Figure 1a. The interconnected Mg-GPE structure is illustrated in Figure 1b. Briefly, PVDF-HFP and Mg[B(hfip)₄]₂ were separately dissolved in dimethoxy

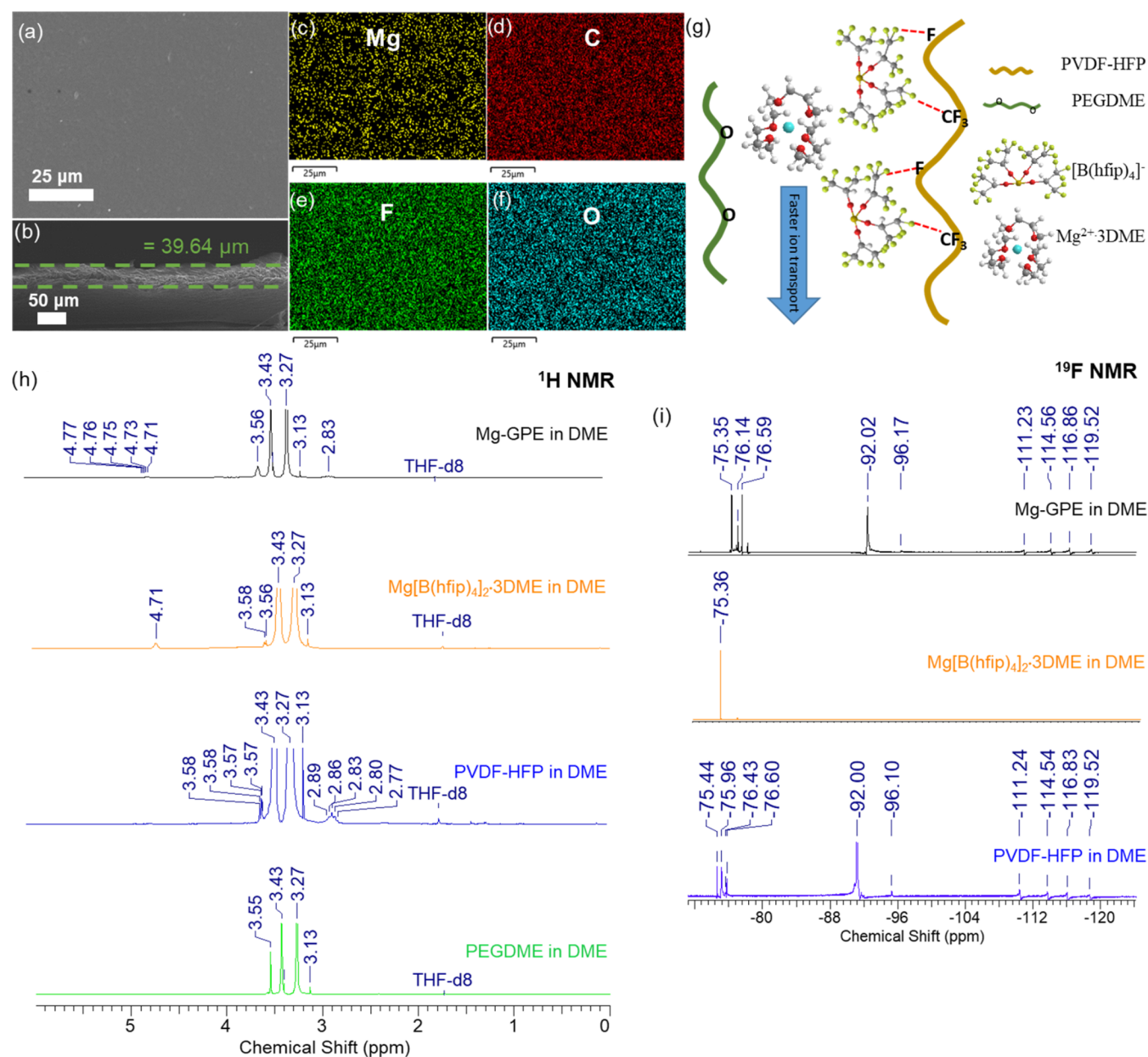


Figure 2. (a) SEM image, (b) cross-sectional SEM image, and (c–f) EDX mappings of the Mg-GPE membrane. (g) Illustration of the interactions between anions and polymer structures in GPE. (h) ^1H NMR (500 MHz, THF-d_8) spectra of Mg-GPE, $\text{Mg}[\text{B}(\text{hfip})_4]_2 \cdot 3\text{DME}$, PVDF-HFP and PEGDME. (i) ^{19}F NMR (471 MHz, THF-d_8) spectra of Mg-GPE, $\text{Mg}[\text{B}(\text{hfip})_4]_2 \cdot 3\text{DME}$, and PVDF-HFP.

ethane (DME) and PEGDME, respectively, and the solutions were then combined. The salt concentration in the electrolyte was maintained at the optimized molar ratio of $-\text{CH}_2\text{CH}_2\text{O}-$ (EO)/Mg = 30:1. When decreasing the EO/Mg ratio, the Mg salt becomes difficult to dissolve in PEGDME. Conversely, using a higher molar ratio makes the film softer, but the reduced Mg salt concentration decreases the current response in the metal stripping/plating tests. After being kept inside a glovebox overnight, the gelation process occurred spontaneously as shown in Figure 1c. In this Mg-GPE system, the EO units function as coordination sites to promote the dissociation of Mg salt. Meanwhile, the EO groups have a high affinity to the liquid electrolyte and effectively entrap solvent molecules in the polymeric framework. The strong solvent-entrapping ability suppresses the leakage and evaporation of the solvent and creates free space in the Mg-GPE to facilitate ion motion

as well as polysulfide dissolution. When pouring the dispersion onto a Petri dish, after several drying steps as described in the Experimental Section, the Mg-GPE membrane was obtained (Figure 1d) and further cut as required for battery assembly. The prepared disks, as shown in Figure 1e,f, exhibit good mechanical flexibility, as they can be bent without cracking, which makes them suitable for applications in bendable batteries.

Scanning electron microscopy (SEM) and energy-dispersive X-ray spectroscopy (EDX) analyses of the Mg-GPE were performed, as shown in Figure 2a–f. The cross-sectional SEM image reveals that the Mg-GPE has an average thickness of about 40 μm . SEM and EDX images confirm a consistent and compact surface, along with a uniform distribution of Mg, C, O, and F elements. This structure is expected to be capable of trapping the dissolved electrode material or electrochemical

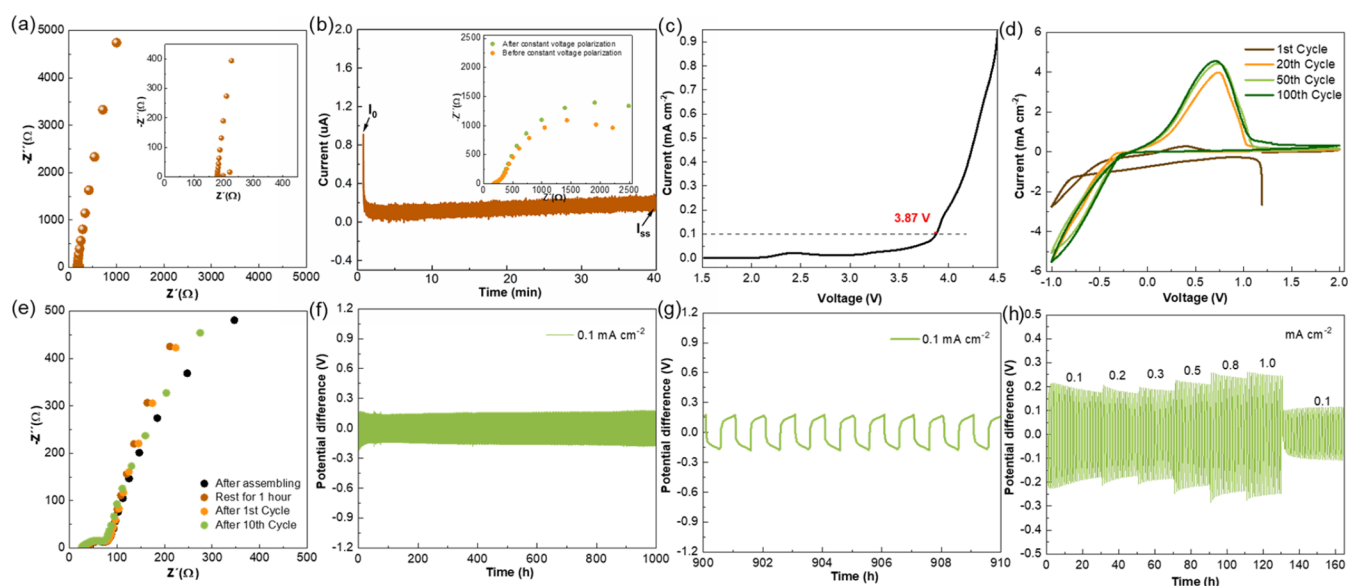


Figure 3. (a) Electrical impedance spectroscopy of a symmetric Al//Mg-GPE//Al cell at 25 °C. The inset shows enlarged profiles in the high-frequency region. (b) DC polarization curve of the Mg symmetrical cell with a total applied potential difference of 10 mV (inset: Nyquist plots of the symmetrical cell before and after DC polarization). (c) Linear sweep voltammetry of an Al//Mg-GPE//Mg cell at a scan rate of 1 mV s⁻¹. (d) Cyclic voltammetry curves for Mg plating and stripping in the Mg-GPE at a sweep rate of 5 mV s⁻¹. (e) Nyquist plots of the symmetrical Mg//Mg-GPE//Mg cell with GPE before cycling, after the 1st and 10th cycles. (f) Long-term cycling of symmetrical Mg//Mg-GPE//Mg cell using Mg-GPE and (g) the enlarged profiles at the 900th to 910th cycles. The current density is 0.1 mA cm⁻², and 0.05 mA h cm⁻² Mg is plated and stripped per cycle. (h) Polarization properties of symmetrical Mg//Mg-GPE//Mg cell at various current densities (from 0.1 to 1.0 mA cm⁻²) for a plating/stripping time of 0.5 h.

intermediates into the polymer matrix. The corresponding EDX analyses for the Mg-GPE membrane and cross-sectional surface mappings of the Mg-GPE are shown in Figures S1–S2, respectively. Except for Mg, boron is another characteristic element of Mg[B(hfip)₄]₂. However, due to its low atomic number, the boron signal is too weak to be reliably detected. Finally, the membrane was soaked in a Mg[B(hfip)₄]₂/DME (0.4 M) solution for 2 h before battery assembly inside a glovebox.

IR spectroscopy and Raman spectroscopy were employed to investigate the interaction of ions with the host polymer and plasticizer in the gel electrolyte system at the molecular level. Figure S3 demonstrates the comparative IR and Raman spectra of the GPE, Mg[B(hfip)₄]₂, PVDF-HFP, and PEGDME. The IR spectra (Figure S3a,b) reveal a shift related to the B–O–C vibration from 1190 to 1181 cm⁻¹ when comparing the spectra of Mg[B(hfip)₄]₂ and the Mg-GPE. In IR spectroscopy, a shift from a higher wavenumber to a lower wavenumber indicates a decrease in the energy of the vibrational mode associated with the bond or functional group. This shift indicates that the coordination environment of the [B(hfip)₄]⁻ anion changes upon entrapment in the polymer host, which will be further confirmed by the following nuclear magnetic resonance (NMR) results. A detailed assignment of all IR bands is listed in Table S1. Additionally, a slight shift in the Raman bands corresponding to the B–O bonds is detected and marked in Figure S3c,d. This shift toward a lower wavenumber in the gel electrolyte, as compared to pristine Mg[B(hfip)₄]₂, serves as additional evidence supporting the presence of an interaction between the polymer and the borate anions. The Raman spectra also indicate that, with the help of the PEGDME plasticizer, the Mg-GPE is highly homogenized with the PVDF-HFP and Mg[B(hfip)₄]₂.

NMR spectra further confirmed the observed interactions. Figure 2h shows the NMR spectra of the Mg-GPE and its individual components (Mg[B(hfip)₄]₂ salt, PVDF-HFP, and PEGDME), all first dissolved in DME and then mixed with THF-*d*₈. In the ¹H NMR spectra, there is a signal for the –CH protons of the [B(hfip)₄]⁻ anions at around 4.71 ppm. Figure S4a,b displays enlarged spectra, highlighting the alterations in the coordination environment of the [B(hfip)₄]⁻ anions. It is hypothesized that some of the anions may interact with the PVDF-HFP polymer and be fixed in the polymer lattice, causing a loss of the chemical equivalence of the hfip units. The H–F interaction could cause a deshielding effect, which leads to a low-field shift. This explanation matches with the position of the additional signal at around 4.76 ppm. The interactions between the Mg[B(hfip)₄]₂ salt, PVDF-HFP, and PEGDME are illustrated in Figure 2g. Additionally, comparable variations in chemical shift were observed in the ¹¹B NMR patterns of the Mg-GPE and Mg[B(hfip)₄]₂ (Figure S4c,d), providing further confirmation of the modified environment of the [B(hfip)₄]⁻ anions.

As shown in the ¹⁹F NMR (Figure 2i), there are signals at around –76 ppm corresponding to the –CF₃ groups in Mg[B(hfip)₄]₂ and PVDF-HFP. Additional signals for the different types of F in PVDF-HFP appear in the range of –92 to –120 ppm. When comparing the ¹⁹F NMR spectra of PVDF-HFP, Mg[B(hfip)₄]₂, and Mg-GPE, most signals in Mg-GPE exhibit minor shift changes. Besides, the main ¹⁹F NMR signal of Mg[B(hfip)₄]₂ shifts slightly toward high field in Mg-GPE. We propose this as a consequence of the deshielding effect of the F–F interaction between the [B(hfip)₄]⁻ anion and the PVDF-HFP polymer. In the case of the PVDF-HFP signals, one part is shifted to high field, while the other part shifts to low field, as summarized in Table S2. A detailed comparison of the zoomed-in regions of ¹⁹F NMR spectra is

also displayed in Figure S5. This phenomenon could be explained by F–F and F–O interactions. When the anion is closer to the PVDF-HFP backbone, both interactions could occur. Unlike the F–F interaction, the F–O interaction leads to a shielding effect and, consequently, a low-field shift.^{33,34} All of these results indicate interactions between the periphery of the $[\text{B}(\text{hfip})_4]^-$ anion and the PVDF-HFP polymer. Due to the beneficial interaction between the $[\text{B}(\text{hfip})_4]^-$ anion and the PVDF-HFP polymer, the Mg-ion transfer can be significantly improved within the GPE despite its much higher viscosity compared to liquid electrolytes. When using polymer electrolytes with multivalent ions, there is often a common issue related to the strong interaction between the polymer and cations, resulting in limited cation mobility.³⁵ In our system, no significant changes were observed in the coordination environment of the cation when comparing the Mg-GPE and liquid electrolyte. This suggests that there is no significant interaction between the Mg cations and the polymer, which might otherwise impede ion transfer. The NMR spectra of Mg-GPE, including ^1H , ^{11}B , and ^{19}F , are summarized in Figure S6.

To investigate the ionic conductivity of the Mg-GPE, electrochemical impedance spectroscopy (EIS) was employed using an aluminum (Al) as ion-blocking electrode, as shown in Figure 3a. Based on the values provided in Table S3, the conductivity was calculated to be $2.92 \times 10^{-5} \text{ S cm}^{-1}$. Another crucial characteristic of an electrolyte, especially for a polymer or solid electrolyte, is the transference number for Mg^{2+} ($t_{\text{Mg}^{2+}}$), which quantifies the fraction of ionic transport. The transference number of the Mg-GPE was determined using the steady-state current method described by Bruce and Vincent,³⁶ (refer to Table S4 in the Supporting Information for detailed information). AC impedance measurements were conducted on the cell both before and after the voltage polarization, and the resulting Nyquist plots are presented in the inset of Figure 3b. The interfacial resistances at the electrode–electrolyte interfaces were determined from the Nyquist plots fitting results, as shown in Figure S7. The $t_{\text{Mg}^{2+}}$ value for the GPE was calculated to be 0.39 ± 0.02 , which is notably comparable to those reported for existing polymer electrolytes used in Li-ion batteries.^{37–39} The high transference number could be attributed to the interaction between the $[\text{B}(\text{hfip})_4]^-$ anion and the gel polymer network, which can hinder the movement of anions while enhancing the Mg^{2+} cation mobility. The electrochemical stability window was determined using linear sweep voltammetry (LSV) with aluminum as the working electrode, as shown in Figure 3c. The current density stayed below 0.1 mA cm^{-2} until reaching a voltage of 3.87 V. Cyclic voltammetry (CV) further validated successful magnesium deposition and stripping on the magnesium electrode with the Mg-GPE and aluminum as the working electrode, as illustrated in Figure 3d. During the initial cycle, there is a conditioning process with low current response, while in the following cycles, the current increased while voltage polarization gradually decreased, indicating faster kinetics and a reversible redox process. Furthermore, to prove that the Mg-GPE allows for successful plating of Mg, plating onto a carbon cloth as the working electrode was demonstrated. For this, a reductive current of 1 mA cm^{-2} was applied to a cell with a carbon cloth as a working electrode and the Mg-GPE for 4 h. From the optical photograph, the formation of shiny gray particles with metallic appearance is clearly visible on the surface of the carbon cloth, as shown in Figure S8b. The X-ray diffraction (XRD) pattern obtained for the carbon cloth after deposition

can be indexed to standard Mg with a hexagonal structure (Figure S8a). The reflection at around 20° can be attributed to the carbon cloth. Furthermore, the SEM images and EDX maps (Figure S8c–h) provide confirmation that the Mg particles were tightly packed and agglomerated on the carbon substrate.

Figure 3e displays the Nyquist plots of the Mg symmetrical cell with the Mg-GPE measured before and after cycling. The compressed semicircle in the high-frequency region of each spectrum is related to the electrode–electrolyte interface impedance, declining after cycling. The low interface resistance can be attributed to the good interfacial compatibility of the Mg-GPE with the electrodes. A galvanostatic cycling test was performed in a Mg symmetrical cell with a current density of 0.1 mA cm^{-2} . As shown in Figure 3f,g, the cell could persevere a low polarization of around 0.10–0.13 V over 1000 cycles. Long-term cycling performance at a high current density of 1.0 mA cm^{-2} was also tested and is demonstrated in Figure S9. The cyclic stability of the cell remained excellent even at high current density, with an overpotential below 0.3 V even after 500 cycles. The results demonstrate that the Mg-GPE allows for efficient plating and stripping of Mg with small overpotentials, leading to an excellent cycling performance that is comparable to or even better than some Mg liquid electrolytes.^{25,40,41} Furthermore, a long-time Mg plating/stripping behavior was achieved in an asymmetrical cell with a plating time of 0.5 h (Figure S10). A consistent Coulombic efficiency of over 90% was achieved after conditioning cycles, which remained stable even after 300 stripping/plating cycles. Figure 3h shows the overpotential values obtained when increasing the current density up to 1.0 mA cm^{-2} . The deposition/stripping overpotential increased slightly with the areal current densities and became stable after few cycles. Even at a relatively high current density of 1.0 mA cm^{-2} , the cell could maintain a low polarization of about 0.26 V. The stable electrochemical performances confirm the uniform deposition of Mg with the help of the Mg-GPE.

In addition, the electrochemical performance of the dry Mg-GPE, which refers to the Mg-GPE without soaking it into liquid electrolyte, was also tested and is presented in Figure S11. It demonstrates an electrochemical stability window of up to 4 V. However, the initial stripping/plating process proves to be challenging, as observed in Figure S11b–d. Notably, in the first cycle of the CV curves, there is no distinct redox peak observed when applying a low voltage limit of -1 V (Figure S11b). Subsequently, the voltage range was extended to -1.5 V , resulting in a weak current response of approximately 0.01 mA cm^{-2} , which progressively increases in the subsequent cycles. The observed low current response and high voltage hysteresis around 4 V (Figure S11d) during the initial cycle are indicative of sluggish kinetics and inadequate mass transport of Mg^{2+} ions within the dry Mg-GPE. As a result, it is necessary to soak the GPE with liquid electrolyte to facilitate sufficient electrochemical reaction kinetics for the stripping and plating of Mg, ensuring the proper functioning of the full cell.

Two test cells were assembled with an additional injection of $20 \mu\text{L}$ of Mg polysulfide (MgS_x) solution to compare the diffusion of polysulfides with different electrolytes. The preparation of the MgS_x solution and the assembly of the two cells are described in the Experimental Section. Here, the Mg-GPE (without an additional separator) was used in one cell, while in the other cell, a liquid electrolyte (with two pieces of glass fiber separator) was employed. Both cells contained a

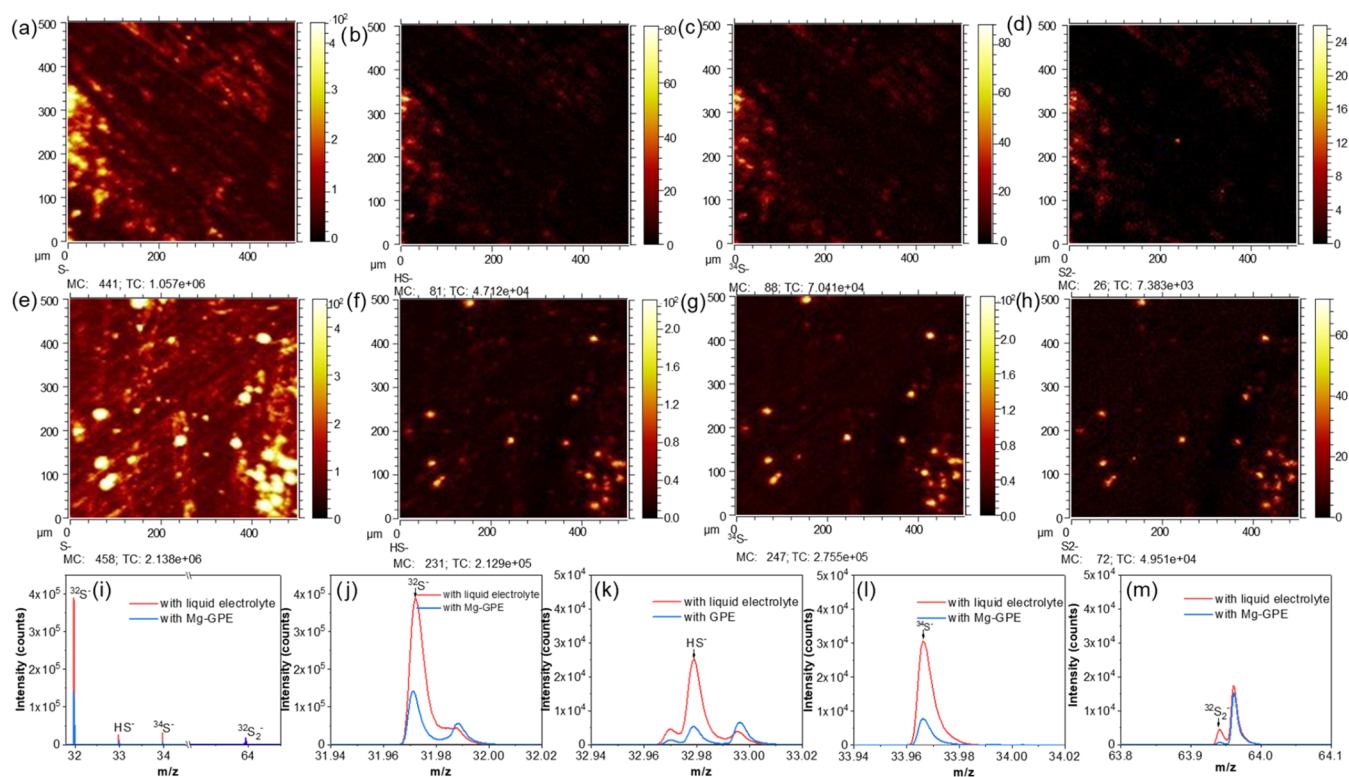


Figure 4. ToF-SIMS depth-integrated images of the ions related to sulfur species on the surface of an electrode with (a–d) the Mg-GPE and (e–h) the liquid electrolyte after 24 h resting. The maximum number of counts in a pixel (MC) and the total number of counts (TC) are indicated below the images. (i–m) The corresponding depth-integrated spectra obtained from these electrodes (red: liquid electrolyte; blue: Mg-GPE).

Mg foil electrode, which was disassembled after 24 h and examined using time-of-flight secondary ion mass spectrometry (ToF-SIMS) to verify the presence of sulfur. Figure 4 presents the depth-integrated images and spectra for both samples. It is evident that the intensity of all of the signals, including $^{32}\text{S}^-$, HS^- , $^{34}\text{S}^-$, and $^{32}\text{S}_2^-$ fragments from sulfur species, is significantly higher in the electrode with the liquid electrolyte (Figure 4e–h) compared to the electrode with the Mg-GPE (Figure 4a–d). Interestingly, in Figure 4e, noticeable spot-like sulfur deposition is observed on the electrode with the liquid electrolyte. This finding aligns with previous reports,⁴² suggesting a reaction between dissolved sulfur species and the Mg anode. A quantitative comparison of sulfur content is presented in Figure 4i–m. The above results clearly demonstrate that, with the protection of the electrode by the Mg-GPE, a much lower amount of sulfur was detected on the electrode. In addition to the ToF-SIMS depth analysis, the ToF-SIMS surface analysis also demonstrated similar results, which further supports the conclusion above. Three different positions were selected on each sample, and the SIMS mapping results for samples with Mg-GPE or liquid electrolyte are presented in Figures S12 and S13, respectively. It is evident that at all selected positions, the sample disassembled from the cell with the liquid electrolyte consistently exhibits higher levels of sulfur species compared to the sample with the Mg-GPE. Overall, ToF-SIMS analyses demonstrate that the Mg-GPE can effectively suppress the diffusion of polysulfides to the anode side.

To further demonstrate the suppression of polysulfide diffusion by Mg-GPE, an H-type glass cell was employed (Figure S14). In this setup, a Mg-GPE was used to separate the left and right chambers of the cell. The left chamber was

injected with a solution of MgS_x in tetraglyme, while the right chamber contained pure tetraglyme solvent. After 1 week, no color was observed in the right chamber. Even after 30 days, the color of the right chamber only changed to a pale yellow. Despite the significant concentration disparity between the two chambers, no apparent polysulfide diffusion was detected within the cell. This confirmed that the Mg-GPE can effectively block polysulfide diffusion.

In the next step, the performance of Mg–S batteries with the Mg-GPE was investigated by employing a model S/C composite as positive and Mg@ACC as negative electrode material. The S/C electrode was fabricated using a commonly used melt-diffusion method, as previously reported.⁴³ SEM and EDX mapping images of the S/C electrode in Figure S15 demonstrate the uniform dispersion of sulfur in the porous carbon fibers. Changes in the open-circuit voltage (OCV) and corresponding impedances of the cell were investigated by separately monitoring the cathode and anode potentials over a resting period with a three-electrode cell as shown in Figure S16. Here, S/C functions as the working electrode (WE), Mg@ACC as the counter electrode (CE), and Mg ring as the reference electrode (RE). After 48 h of rest, the potential change of both the WE and CE was less than 0.1 V. As well known in Mg–S batteries, they suffer from serious self-discharge behavior with a sharply declining OCV in liquid electrolyte, as reported.^{22,44} The stable OCV validates that the Mg-GPE can effectively suppress the dissolution and the diffusion of polysulfide, thus protecting the negative electrode from parasitic reactions of the dissolved sulfur species. The Nyquist plots demonstrate the growth trends of both cathode and anode impedance with resting time, which may relate to an adsorption layer formation on the electrode surfaces.

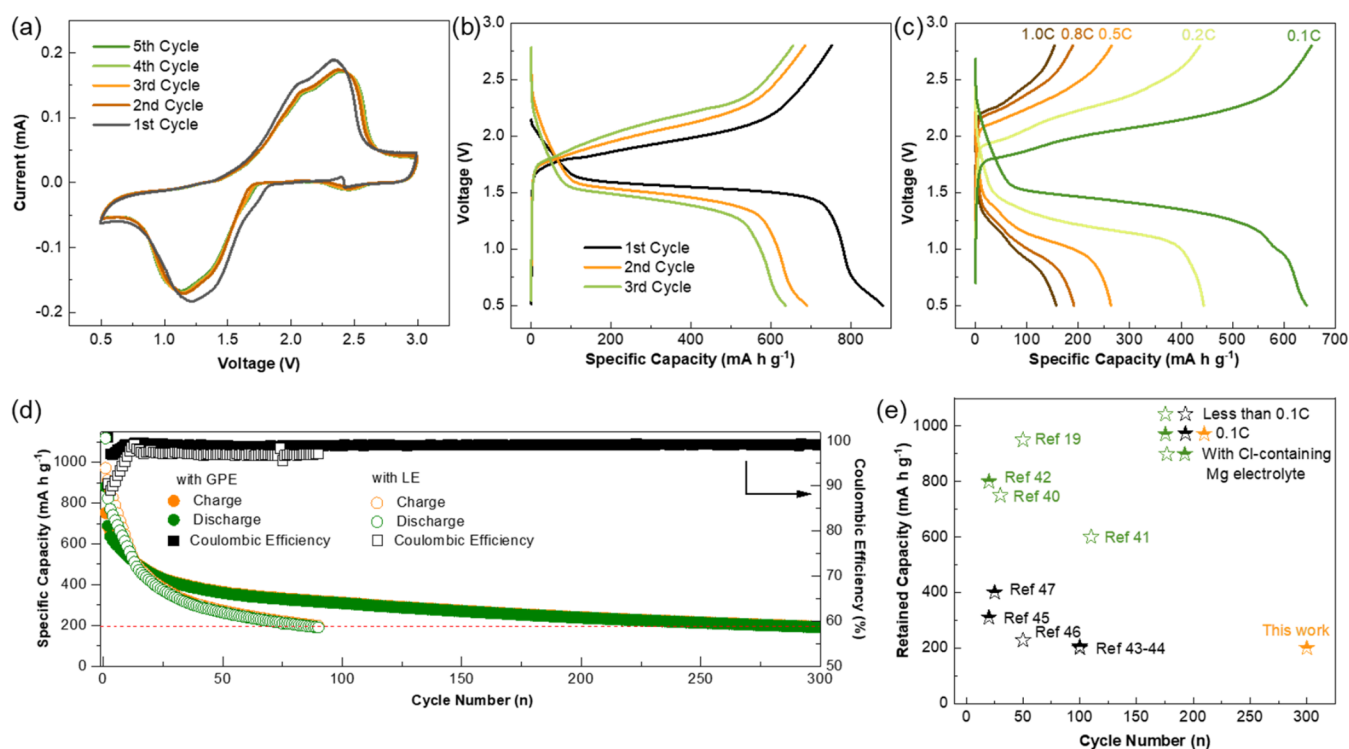


Figure 5. (a) CVs of a Mg–S coin cell with the Mg–GPE at a scan rate of 0.1 mV s^{-1} for the first five cycles. (b) Galvanostatic discharge/charge curves of the Mg–S cell for the first three cycles. (c) Rate performance of Mg–S cell at C-rates of 0.1C, 0.2C, 0.5C, 0.8C, and 1C. (d) Comparison of cycling performance of cells with the Mg–GPE and $0.4 \text{ M Mg[B(hfp)}_4\text{]}_2 \cdot 3\text{DME}$ in DME as liquid electrolyte at 0.1C. (e) Comparison of different Mg–S cells with regard to their cycle numbers and retained capacities including this work.^{24,45–52} The corresponding values are listed in Table S5.

The cyclic voltammetry curves of the Mg–S cell are presented in Figure 5a. During the first cathodic scan, the main reduction peak emerged at around 1.25 V, while the oxidation peak appeared at around 2.20–2.35 V, which is consistent with the plateaus observed in the charge/discharge profiles (Figure 5b). From the second cycle onward, the curves overlap, indicating stable charge/discharge behavior of the system. The reaction kinetics were further investigated through capacity tests at different C-rates (Figure 5c). Due to limited contact between the electrodes and the Mg–GPE (compared to a liquid electrolyte (LE)), there is a gap between the low C rate of 0.2C and the higher one of 0.5C. The corresponding Coulombic efficiencies at different C-rates are shown in Figure S17. The cycling performances of Mg–S cells with both Mg–GPE and liquid electrolyte were evaluated and compared at a 0.1C rate shown in Figure 5d. When using the liquid electrolyte, a higher initial capacity was achieved, which can be attributed to the improved wettability and enhanced electrode–electrolyte contact. However, the capacity exhibited a rapid decline within the first 20 cycles, resulting in a capacity retention below 200 mA h g^{-1} within 90 cycles. A long-term cycling performance of the Mg–S cell with liquid electrolyte is demonstrated in Figure S18. In contrast, the utilization of Mg–GPE significantly extended the cycle life of the Mg–S cell to 300 cycles, while maintaining a discharge capacity above 200 mA h g^{-1} . As demonstrated in Figure 5e and Table S5, the majority of the reported Mg–S batteries exhibit high capacities when employing Cl-containing Mg electrolyte.^{24,45–47} However, the long-term cycling durability of these batteries is limited due to the corrosive nature of Cl⁻ ions, which may affect the compatibility of the electrolytes with conventional

metallic current collectors and other battery components. The Cl-free Mg–GPE is able to maintain a comparable capacity retention while significantly extending the life span of Mg–S batteries, making the Mg–GPE a promising electrolyte candidate. Further research is needed to enhance the capacity retention, especially during the initial 20 cycles, which may relate to some interfacial issues between electrodes and the GPE.

To explore the capacity contribution of the ACC current collector, coin cells were assembled with pure ACC and a Mg anode. Galvanostatic charge/discharge experiments were performed in a voltage range of 0.5–2.5 V vs Mg/Mg²⁺ and at a current of $167.5 \mu\text{A}$ (corresponding to 0.1C with 1 mg sulfur as active material) as shown in Figure S19. This demonstrated that ACC exhibits capacitor-like behavior and can contribute a specific capacity of approximately 40 mA h g^{-1} . Finally, post-mortem SEM images and EDX maps of the Mg@ACC electrode after cycling with the Mg–GPE are shown in Figure S20. The SEM images indicate that the structure of the Mg@ACC electrode was maintained. On its surface that was in direct contact with the Mg–GPE, there is a slight change in the morphology of the Mg metal, indicating a shift in the growth orientation of Mg due to the influence of the Mg–GPE. Additionally, no extra sulfur signal was detected via EDX, confirming the effective suppression of polysulfide shuttle by the Mg–GPE.

Density functional theory (DFT) calculations were conducted to investigate the impact of poly(ethylene glycol) (PEG) on the coordination environment of Mg²⁺ in Mg–GPE. The difference in solvation structure will result in divergent electrochemical performance, such as ionic conductivity and

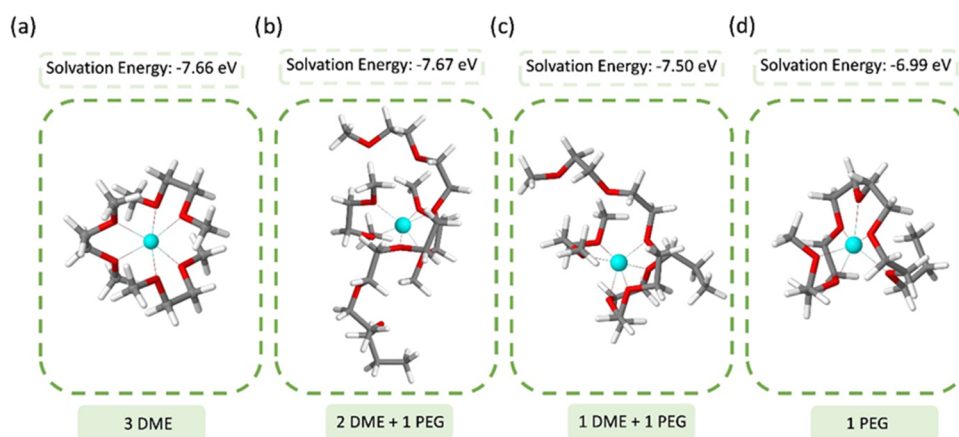


Figure 6. Solvated structure of Mg^{2+} with (a) three DME molecules, (b) two DME molecules and PEG chain, (c) one DME molecule and PEG chain, and (d) PEG chain. The colors correspond to the elements: cyan—magnesium, red—oxygen, gray—carbon, white—hydrogen.

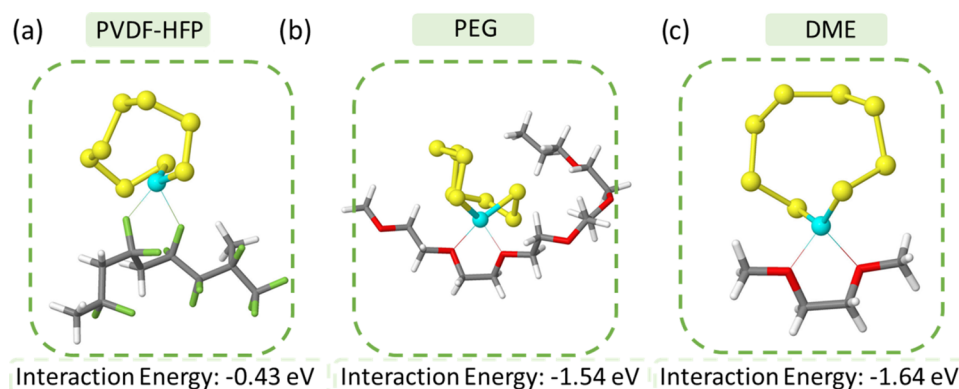


Figure 7. Optimized structures of interactions of MgS_8 with (a) PVDF-HFP, (b) PEG, and (c) DME. The colors correspond to the elements: cyan—magnesium, red—oxygen, gray—carbon, white—hydrogen, green—fluorine.

diffusion coefficient. A previous study has demonstrated that in a liquid electrolyte with DME solvent, Mg^{2+} tends to coordinate with three molecules of DME, resulting in coordination numbers of six.⁵³ Therefore, we computed the solvation energy of six-fold coordinated Mg^{2+} with DME and PEG. The corresponding solvation structures with solvation energies are illustrated in Figure 6a,d. We also calculated the solvation energy for two possible intermediate solvation structures for Mg^{2+} involving DME and PEG simultaneously by gradually removing the DME molecules and solvating the Mg^{2+} ion with two oxygen atoms of the PEG for each DME eliminated (Figure 6b,c). Although the change in coordination environment by substituting one DME molecule with two oxygen atoms of PEG does not significantly alter the solvation energy, further replacing the DME molecule with oxygen atoms of PEG results in a decrease in solvation energy. The weakened solvation when Mg^{2+} ions are solvated with a majority of oxygen atoms from PEG implies that the transportation of Mg^{2+} will be facilitated in Mg-GPE.

Further investigation was conducted into the interaction between the Mg-GPE and polysulfide using DFT calculations, with MgS_8 chosen as a representative example of a polysulfide. The interaction energy between MgS_8 and PVDF-HFP, PEG, or DME was evaluated, yielding values of -0.43 , -1.54 , and -1.64 eV, respectively (Figure 7). While the interaction energy with PVDF-HFP is weak, both DME and PEG exhibit strong interactions with polysulfides. Being a polymer chain, PEG tends to anchor the MgS_8 , impeding the diffusion of

polysulfides. On the other hand, DME, being mobile, may facilitate the transport of polysulfides. Therefore, we conclude that the presence of the PEGDME polymer within the Mg-GPE can anchor the polysulfides, hinder their transport, and reduce the shuttling effect compared to a liquid electrolyte containing only DME solvent.

CONCLUSIONS

In this work, we presented a free-standing Mg-GPE for long-cycle-life Mg batteries using a solvent-casting method. The Mg-GPE not only enables a uniform deposition of Mg but also effectively inhibits the dissolution and diffusion of electrochemical reaction intermediates. In the symmetric cell with the Mg-GPE, a stable plating/stripping behavior of Mg was observed over 1000 cycles. In a Mg-S battery with the Mg-GPE, remarkable and unprecedented stability over 300 cycles resulted in a retained capacity of 200 mA h g^{-1} . These significant enhancements in stability suggest that GPE holds great promise in achieving reversible metal deposition/dissolution and addressing the current limitations of RMBs. Moreover, it also paves the way for the development of next-generation RMBs with high performance, superior safety, and enhanced flexibility.

EXPERIMENTAL SECTION

Mg-Based Gel Polymer Electrolyte (Mg-GPE) Synthesis.

Commercially available poly(vinylidene fluoride-co-hexafluoropropylene) (PVDF-HFP, Aldrich, average M_w of $400,000 \text{ g mol}^{-1}$) and

poly(ethylene glycol) dimethyl ether (PEGDME, Aldrich, average M_w of 500 g mol⁻¹) were used as received. Anhydrous dimethoxy ethane (DME, Sigma) was stored over 3 Å molecular sieves in a glovebox overnight before use. The magnesium tetrakis-(hexafluoroisopropoxy)borate ($Mg[B(hfip)_4]_2$) electrolyte was synthesized through a reaction between $Mg(BH_4)_2$ and hexafluoroisopropanol ((CF_3)₂CHOH, 99%, Alfa Aesar) in DME, as previously reported.⁴⁹ A 0.4 M liquid electrolyte solution was prepared by dissolving the appropriate amount of magnesium salt in DME, with the concentration based on the molecular weight of $Mg[B(hfip)_4]_2 \cdot 3DME$.

Free-standing polymer electrolyte films were prepared by solution-casting in an argon-filled glovebox. First, 400 mg of PVDF-HFP was dissolved in 3 mL of DME and stirred intensely at 80 °C for 4 h (=solution A). The $Mg[B(hfip)_4]_2 \cdot 3DME$ salt was dissolved in PEGDME (=solution B) at a ratio of 30 EO units per Mg^{2+} cation. Solution B was then added to solution A and stirred for 30 min to form the final gel solution. The gel solution was cast into a Petri dish (6 cm diameter) at room temperature for 12 h to evaporate the bulk solvent and further dried at 80 °C for another 12 h. The weight ratio of PVDF-HFP within the GPE membrane is 22.4%. Finally, the resulting polymer film was cut into disks with a diameter of 16 mm (for coin cell) or 22 mm (for three-electrode cell) and infiltrated with 0.4 M $Mg[B(hfip)_4]_2 \cdot 3DME$ in DME liquid electrolyte overnight before use.

Preparation of Mg@ACC Electrode. A galvanostatic electrodeposition method was used to prepare Mg@ACC electrodes as reported in our previous work.⁵⁴ Before the electrodeposition process, the activated carbon cloth (ACC-507-20, Kynol Europa GmbH) was cut into disks with a diameter of 13 mm and vacuum-dried at 230 °C overnight. CR2032-type coin cells were assembled to deposit Mg on the ACC. The coin cells consisted of a Mg foil as the counter/reference electrode, two pieces of polypropylene monolayer separator (Celgard 2500) in between, and a piece of ACC as the working electrode. The smooth surface of the Celgard separator ensures easy peel-off after electrodeposition. Prior to cell assembly, the Mg foil (0.1 mm, Gelon Energy Corp) was cut into disks with a 14 mm diameter and carefully scratched on both sides in the glovebox to remove the native oxide layer from its surface. The electrodeposition was performed at a discharge current density of 1 mA cm⁻² for 4 h and stabilized at approximately 0.25 V vs Mg^{2+}/Mg in the electrolyte containing 0.4 M $Mg[B(hfip)_4]_2 \cdot 3DME$ in DME.

Then Mg@ACC electrode was obtained by disassembling the coin cells after the electrodeposition process and used as the negative electrode in all of the cells tested in this work.

Preparation of Magnesium Polysulfides (MgS_x) Solution. 2.053 g (64.0 mmol) of elemental sulfur powder (99.98%, Sigma-Aldrich) and 0.194 g (8.0 mmol) of Mg crumbs scratched off a Mg foil were added to a glass vial and mixed with 30 mL of tetraglyme in a glovebox. The suspension was stirred at 60 °C for 3 days. Finally, the suspension was filtered and the resulting reddish polysulfide solution was used for H-cell testing, as shown in Figure S14.

Preparation of the S/C Electrode. The preparation of S/C composite was carried out according to previously published protocols.^{43,46} The activated carbon cloth was first cut into circular disks with a diameter of 10 mm and dried under vacuum at 230 °C overnight. Elemental sulfur powder was homogeneously dispersed on the carbon disks. The disks were then transferred to a glass tube with a diameter of 1 cm, which was subsequently sealed under vacuum and heated to 160 °C for 16 h. The sulfur loading was calculated by subtracting the mass of the blank activated carbon cloth from the mass of the loaded electrode to be, around 1.0 mg cm⁻².

Characterization. X-ray diffraction (XRD) measurements were conducted on an STOE STADI diffractometer with a Mo $K\alpha$ X-ray source operated at 50 kV and 40 mA in the range of 10–40°. Scanning electron microscopy (SEM) images were obtained using a ZEISS LEO 1530 at 10 kV electron beam with energy-dispersive X-ray spectroscopy (EDX). The SEM samples were prepared on carbon tapes. IR characterization was performed inside the glovebox using a Spectrum Two FT-IR Spectrometer (PerkinElmer). The spectra were

measured by using the ATR mode. Measurements were collected in the range between 4000 and 500 cm⁻¹ at room temperature. ¹H, ¹¹B, and ¹⁹F nuclear magnetic resonance (NMR) spectra were measured on a Bruker Advance II 500 spectrometer. THF-*d*₈ was used as a solvent for NMR measurements, and the chemical shifts are reported in ppm using one residual solvent peak at 1.73 ppm as the reference. Raman measurements were carried out with a confocal Raman microscope (InVia, Renishaw) in the spectral range of 200–3200 cm⁻¹ using a 532 nm laser excitation source. Time-of-flight secondary ion mass spectrometry (ToF-SIMS) was performed on a TOF-SIMS instrument (ION-TOF GmbH) equipped with a Bi cluster primary ion source and a reflection-type time-of-flight analyzer. UHV base pressure was <2 × 10⁻⁸ mbar. For high mass resolution, the primary ion source was operated in “high current bunched” mode providing short Bi₃⁺ primary ion pulses for static SIMS imaging or Bi⁺ for depth profiling (25 keV). The short pulse length of 1.0 ns allowed for high mass resolution. The primary ion beam was scanned across a 500 × 500 μm² field of view on the sample, and 128 × 128 data points were recorded. Primary ion doses were kept below 10¹¹ ions/cm² (static SIMS limit). Spectra were calibrated on the omnipresent C⁻, CH⁻, CH₂⁻, C₂⁻, and S⁻ peaks. For depth profiling, a dual beam analysis was performed in interlaced mode: The primary ion source was again operated in “high current bunched” mode with a scanned area of 500 × 500 μm² and a sputter gun (operated with Cs⁺ ions, 2 keV, scanned over a concentric field of 750 × 750 μm², target current 135–157 nA) was applied to erode the sample up to a total fluence of >1.1 × 10¹⁷ ions/cm² passing through the surface layer on the samples.

Electrochemical measurements. The CR2032 coin cells and three-electrode cells (PAT-Cell, EL-CELL) were assembled in an argon-filled glovebox (H₂O, O₂ < 0.1 ppm). The glass fiber ((GF/C) from Whatman) membranes were vacuum-dried at 230 °C overnight and were used as a separator. Symmetric and asymmetric cells were employed to evaluate the cycling stability and cycle life span of the negative electrodes. During the electrochemical process, Mg was continuously plated or stripped at a current density of 0.1 mA cm⁻². Electrochemical impedance spectroscopy (EIS) was carried out on an electrochemical workstation (VMP-3 Biologic) from 1 MHz to 20 mHz with a DC voltage amplitude of 10 mV.

Two coin cells were assembled for the ToF-SIMS test, with Mg foil serving as the negative electrode and a stainless steel current collector as the positive electrode. Between the electrodes, one cell had a Mg-GPE membrane, while the other cell had two pieces of glass fiber separators (Whatman GF/C) along with 80 μL of 0.4 M $Mg[B(hfip)_4]_2 \cdot 3DME$ in DME liquid electrolyte. Additionally, 20 μL of MgS_x solution was injected into both cells. Both cells were kept 24 h inside the glovebox before the ToF-SIMS test.

For the Mg-S coin cells, galvanostatic charge/discharge experiments were performed in a voltage range of 0.5–2.7 V vs Mg/Mg^{2+} and at a C rate of 0.1C (S: 1C = 1675 mA g⁻¹). Cyclic voltammetry (CV) measurements were carried out at a scan rate of 0.1 mV s⁻¹ in a voltage range of 0.5–3.0 V vs Mg/Mg^{2+} on a Biologic VMP-3 potentiostat. All electrochemical investigations were conducted at 25 °C.

DFT Calculations. All DFT calculations are performed using the Amsterdam density functional (ADF) package as implemented in the Amsterdam modeling suite (AMS).⁵⁵ The geometries of all of the molecular systems are optimized using M06-2X meta-hybrid functional and TZP basis set. The influence of the surrounding liquid is simulated using the COSMO solvation model with dielectric constant 7.2 that corresponds to DME.⁵⁶ The calculations involving polymers employed short oligomers to mimic the polymer chain. The interaction energy is calculated as the difference between the energy of the complexes and the separate molecules. Similarly, the solvation energy is calculated as the difference between the energy of the solvated structure and the separate molecules.

■ ASSOCIATED CONTENT

SI Supporting Information

The Supporting Information is available free of charge at <https://pubs.acs.org/doi/10.1021/acsaem.4c01049>.

Material characterization, electrochemical measurements, SEM images, EDX spectra and mapping images, ToF-SIMS images, IR spectra, Raman spectra, NMR spectra, optical images of the diffusion of polysulfides with visualized H-type glass devices, EIS analysis, cyclic performance, summary of the conductivities with different electrolyte, and comparison of electrochemical performances of different Mg–S cells (PDF)

■ AUTHOR INFORMATION

Corresponding Author

Liping Wang – Institute of Organic Chemistry II and Advanced Materials, Ulm University, 89081 Ulm, Germany; orcid.org/0000-0002-4113-2208; Email: liping.wang@partner.kit.edu, liping-l.wang@uni-ulm.de

Authors

- Sibylle Riedel – Helmholtz Institute Ulm (HIU), Electrochemical Energy Storage, Ulm 89081, Germany
- Alexander Welle – Karlsruhe Nano Micro Facility, and Institute of Functional Interfaces (IFG), Karlsruhe Institute of Technology (KIT), Eggenstein-Leopoldshafen 76344, Germany; orcid.org/0000-0002-3454-6509
- Smobin Vincent – Department of Energy Conversion and Storage, Technical University of Denmark, Kongens Lyngby DK-2800, Denmark; orcid.org/0000-0002-6147-4360
- Sirshendu Dinda – Helmholtz Institute Ulm (HIU), Electrochemical Energy Storage, Ulm 89081, Germany
- Bosubabu Dasari – Helmholtz Institute Ulm (HIU), Electrochemical Energy Storage, Ulm 89081, Germany; orcid.org/0000-0001-8816-2984
- Juan Maria Garcia Lastra – Department of Energy Conversion and Storage, Technical University of Denmark, Kongens Lyngby DK-2800, Denmark; orcid.org/0000-0001-5311-3656
- Birgit Esser – Institute of Organic Chemistry II and Advanced Materials, Ulm University, 89081 Ulm, Germany; orcid.org/0000-0002-2430-1380
- Zhirong Zhao-Karger – Helmholtz Institute Ulm (HIU), Electrochemical Energy Storage, Ulm 89081, Germany; Karger Institute of Nanotechnology, Karlsruhe Institute of Technology (KIT), Eggenstein-Leopoldshafen 76344, Germany; orcid.org/0000-0002-7233-9818

Complete contact information is available at: <https://pubs.acs.org/doi/10.1021/acsaem.4c01049>

Notes

The authors declare no competing financial interest.

■ ACKNOWLEDGMENTS

This work contributes to the research performed at CELEST (Center for Electrochemical Energy Storage Ulm-Karlsruhe) and was funded by the German Research Foundation (DFG) under Project ID 390874152 (POLiS Cluster of Excellence, EXC 2154).

■ REFERENCES

- (1) Mohtadi, R.; Tutusaus, O.; Arthur, T. S.; Zhao-Karger, Z.; Fichtner, M. The metamorphosis of rechargeable magnesium batteries. *Joule* **2021**, *5* (3), 581–617.
- (2) Gregory, T. D.; Hoffman, R. J.; Winterton, R. C. Nonaqueous electrochemistry of magnesium: applications to energy storage. *J. Electrochem. Soc.* **1990**, *137* (3), No. 775.
- (3) Yoo, H. D.; Shterenberg, I.; Gofer, Y.; Gershtinsky, G.; Pour, N.; Aurbach, D. Mg rechargeable batteries: an on-going challenge. *Energy Environ. Sci.* **2013**, *6* (8), 2265–2279.
- (4) Davidson, R.; Verma, A.; Santos, D.; Hao, F.; Fincher, C.; Xiang, S.; Van Buskirk, J.; Xie, K.; Pharr, M.; Mukherjee, P. P.; Banerjee, S. Formation of Magnesium Dendrites during Electrodeposition. *ACS Energy Lett.* **2019**, *4* (2), 375–376.
- (5) Aurbach, D.; Cohen, Y.; Moshkovich, M. The Study of Reversible Magnesium Deposition by In Situ Scanning Tunneling Microscopy. *Electrochem. Solid-State Lett.* **2001**, *4* (8), No. A113.
- (6) Zhao, Q. S.; NuLi, Y. N.; Guo, Y. S.; Yang, J.; Wang, J. L. Reversibility of electrochemical magnesium deposition from tetrahydrofuran solutions containing pyrrolidinyll magnesium halide. *Electrochim. Acta* **2011**, *56* (18), 6530–6535.
- (7) Jäckle, M.; Groß, A. Microscopic properties of lithium, sodium, and magnesium battery anode materials related to possible dendrite growth. *J. Chem. Phys.* **2014**, *141* (17), No. 174710.
- (8) Jäckle, M.; Helmbrecht, K.; Smits, M.; Stottmeister, D.; Groß, A. Self-diffusion barriers: possible descriptors for dendrite growth in batteries? *Energy Environ. Sci.* **2018**, *11* (12), 3400–3407.
- (9) Muldoon, J.; Bucur, C. B.; Gregory, T. Fervent Hype behind Magnesium Batteries: An Open Call to Synthetic Chemists—Electrolytes and Cathodes Needed. *Angew. Chem., Int. Ed.* **2017**, *56* (40), 12064–12084.
- (10) Ma, Z.; Macfarlane, D. R.; Kar, M. Mg Cathode Materials and Electrolytes for Rechargeable Mg Batteries: A Review. *Batteries Supercaps* **2019**, *2* (2), 115–127.
- (11) Erickson, E. M.; Markevich, E.; Salitra, G.; Sharon, D.; Hirshberg, D.; de la Llave, E.; Shterenberg, I.; Rosenman, A.; Frimer, A.; Aurbach, D. Review—Development of Advanced Rechargeable Batteries: A Continuous Challenge in the Choice of Suitable Electrolyte Solutions. *J. Electrochem. Soc.* **2015**, *162* (14), No. A2424.
- (12) Aurbach, D.; Gizbar, H.; Schechter, A.; Chusid, O.; Gottlieb, H. E.; Gofer, Y.; Goldberg, I. Electrolyte Solutions for Rechargeable Magnesium Batteries Based on Organomagnesium Chloroaluminate Complexes. *J. Electrochem. Soc.* **2002**, *149* (2), A115–A121.
- (13) Lu, Z.; Schechter, A.; Moshkovich, M.; Aurbach, D. On the electrochemical behavior of magnesium electrodes in polar aprotic electrolyte solutions. *J. Electroanal. Chem.* **1999**, *466* (2), 203–217.
- (14) Hu, M.; Li, G.; Chen, K.; Zhou, X.; Li, C. A gradient structured SEI enabling record-high areal capacity anode for high-rate Mg metal batteries. *Chem. Eng. J.* **2024**, *480*, No. 148193.
- (15) Zhou, X.; Li, G.; Yu, Y.; Lei, M.; Chen, K.; Li, C. Building Organic–Inorganic Robust Interphases from Deep Eutectic Solution for Highly Stable Mg Metal Anode in Conventional Electrolyte. *Small Methods* **2023**, No. 2301109.
- (16) Li, Y.; Zhou, X.; Hu, J.; Zheng, Y.; Huang, M.; Guo, K.; Li, C. Reversible Mg metal anode in conventional electrolyte enabled by durable heterogeneous SEI with low surface diffusion barrier. *Energy Storage Mater.* **2022**, *46*, 1–9.
- (17) Yao, Z.; Yu, Y.; Wu, Q.; Cui, M.; Zhou, X.; Liu, J.; Li, C. Maximizing Magnesium Capacity of Nanowire Cluster Oxides by Conductive Macromolecule Pillaring and Multication Intercalation. *Small* **2021**, *17* (30), No. 2102168.
- (18) Levi, E.; Gofer, Y.; Aurbach, D. On the Way to Rechargeable Mg Batteries: The Challenge of New Cathode Materials. *Chem. Mater.* **2010**, *22* (3), 860–868.
- (19) Kim, H. S.; Arthur, T. S.; Allred, G. D.; Zajicek, J.; Newman, J. G.; Rodnyansky, A. E.; Oliver, A. G.; Boggess, W. C.; Muldoon, J. Structure and compatibility of a magnesium electrolyte with a sulphur cathode. *Nat. Commun.* **2011**, *2* (1), No. 427.

- (20) Rashad, M.; Asif, M.; Ali, Z. Quest for magnesium-sulfur batteries: Current challenges in electrolytes and cathode materials developments. *Coord. Chem. Rev.* **2020**, *415*, No. 213312.
- (21) Kong, L.; Yan, C.; Huang, J.-Q.; Zhao, M.-Q.; Titiirci, M.-M.; Xiang, R.; Zhang, Q. A Review of Advanced Energy Materials for Magnesium–Sulfur Batteries. *Energy Environ. Mater.* **2018**, *1* (3), 100–112.
- (22) Ford, H. O.; Doyle, E. S.; He, P.; Boggess, W. C.; Oliver, A. G.; Wu, T.; Sterbinsky, G. E.; Schaefer, J. L. Self-discharge of magnesium–sulfur batteries leads to active material loss and poor shelf life. *Energy Environ. Sci.* **2021**, *14* (2), 890–899.
- (23) Parambath, V. B.; Zhao-Karger, Z.; Diemant, T.; Jäckle, M.; Li, Z.; Scherer, T.; Gross, A.; Behm, R. J.; Fichtner, M. Investigation on the formation of Mg metal anode/electrolyte interfaces in Mg/S batteries with electrolyte additives. *J. Mater. Chem. A* **2020**, *8* (43), 22998–23010.
- (24) Xu, Y.; Zhou, G.; Zhao, S.; Li, W.; Shi, F.; Li, J.; Feng, J.; Zhao, Y.; Wu, Y.; Guo, J.; Cui, Y.; Zhang, Y. Improving a Mg/S Battery with YCl₃ Additive and Magnesium Polysulfide. *Adv. Sci.* **2019**, *6* (4), No. 1800981.
- (25) Fan, H.; Zheng, Z.; Zhao, L.; Li, W.; Wang, J.; Dai, M.; Zhao, Y.; Xiao, J.; Wang, G.; Ding, X.; Xiao, H.; Li, J.; Wu, Y.; Zhang, Y. Extending Cycle Life of Mg/S Battery by Activation of Mg Anode/Electrolyte Interface through an LiCl-Assisted MgCl₂ Solubilization Mechanism. *Adv. Funct. Mater.* **2019**, *30* (9), No. 1909370.
- (26) Wang, W. P.; Zhang, J.; Chou, J.; Yin, Y. X.; You, Y.; Xin, S.; Guo, Y. G. Solidifying Cathode–Electrolyte Interface for Lithium–Sulfur Batteries. *Adv. Energy Mater.* **2021**, *11*, No. 2000791.
- (27) Qian, J.; Jin, B.; Li, Y.; Zhan, X.; Hou, Y.; Zhang, Q. Research progress on gel polymer electrolytes for lithium-sulfur batteries. *J. Energy Chem.* **2021**, *56*, 420–437.
- (28) Fan, H.; Zhao, Y.; Xiao, J.; Zhang, J.; Wang, M.; Zhang, Y. A non-nucleophilic gel polymer magnesium electrolyte compatible with sulfur cathode. *Nano Res.* **2020**, *13* (10), 2749–2754.
- (29) Ford, H. O.; Merril, L. C.; He, P.; Upadhyay, S. P.; Schaefer, J. L. Cross-Linked Ionomer Gel Separators for Polysulfide Shuttle Mitigation in Magnesium–Sulfur Batteries: Elucidation of Structure–Property Relationships. *Macromolecules* **2018**, *51* (21), 8629–8636.
- (30) Wang, L. P.; Li, Z. Y.; Meng, Z.; Xiu, Y. L.; Dasari, B.; Zhao-Karger, Z.; Fichtner, M. Designing gel polymer electrolyte with synergetic properties for rechargeable magnesium batteries. *Energy Storage Mater.* **2022**, *48*, 155–163.
- (31) Fasciani, C.; Panero, S.; Hassoun, J.; Scrosati, B. Novel configuration of poly(vinylidene difluoride)-based gel polymer electrolyte for application in lithium-ion batteries. *J. Power Sources* **2015**, *294*, 180–186.
- (32) Castillo, J.; Santiago, A.; Judez, X.; Garbayo, I.; Clemente, J. A. C.; Morant-Miñana, M. C.; Villaverde, A.; González-Marcos, J. A.; Zhang, H.; Armand, M.; Li, C. Safe, Flexible, and High-Performing Gel-Polymer Electrolyte for Rechargeable Lithium Metal Batteries. *Chem. Mater.* **2021**, *33* (22), 8812–8821.
- (33) Dalvit, C.; Vulpetti, A. Fluorine–Protein Interactions and 19F NMR Isotropic Chemical Shifts: An Empirical Correlation with Implications for Drug Design. *ChemMedChem* **2011**, *6* (1), 104–114.
- (34) Dolbier, W. R. An Overview of Fluorine NMR. In *Guide to Fluorine NMR for Organic Chemists*; John Wiley & Sons, 2009; pp 9–53.
- (35) Park, B.; Schaefer, J. L. Review—Polymer Electrolytes for Magnesium Batteries: Forging Away from Analogs of Lithium Polymer Electrolytes and Towards the Rechargeable Magnesium Metal Polymer Battery. *J. Electrochem. Soc.* **2020**, *167* (7), No. 070545.
- (36) Evans, J.; Vincent, C. A.; Bruce, P. G. Electrochemical measurement of transference numbers in polymer electrolytes. *Polymer* **1987**, *28* (13), 2324–2328.
- (37) Deivanayagam, R.; Cheng, M.; Wang, M.; Vasudevan, V.; Foroozan, T.; Medhekar, N. V.; Shahbazian-Yassar, R. Composite Polymer Electrolyte for Highly Cyclable Room-Temperature Solid-State Magnesium Batteries. *ACS Appl. Energy Mater.* **2019**, *2* (11), 7980–7990.
- (38) Du, A.; Zhang, H.; Zhang, Z.; Zhao, J.; Cui, Z.; Zhao, Y.; Dong, S.; Wang, L.; Zhou, X.; Cui, G. A Crosslinked Polytetrahydrofuran-Borate-Based Polymer Electrolyte Enabling Wide-Working-Temperature-Range Rechargeable Magnesium Batteries. *Adv. Mater.* **2019**, *31* (11), No. 1805930.
- (39) Anilkumar, K. M.; Jinisha, B.; Manoj, M.; Jayalekshmi, S. Poly(ethylene oxide) (PEO) – Poly(vinyl pyrrolidone) (PVP) blend polymer based solid electrolyte membranes for developing solid state magnesium ion cells. *Eur. Polym. J.* **2017**, *89*, 249–262.
- (40) Du, A.; Zhang, Z.; Qu, H.; Cui, Z.; Qiao, L.; Wang, L.; Chai, J.; Lu, T.; Dong, S.; Dong, T.; Xu, H.; Zhou, X.; Cui, G. An efficient organic magnesium borate-based electrolyte with non-nucleophilic characteristics for magnesium–sulfur battery. *Energy Environ. Sci.* **2017**, *10* (12), 2616–2625.
- (41) Zhao, X.; Yang, Y.; NuLi, Y.; Li, D.; Wang, Y.; Xiang, X. A new class of electrolytes based on magnesium bis(diisopropyl)amide for magnesium-sulfur batteries. *Chem. Commun.* **2019**, *55* (43), 6086–6089.
- (42) Gao, T.; Hou, S.; Huynh, K.; Wang, F.; Eidson, N.; Fan, X.; Han, F.; Luo, C.; Mao, M.; Li, X.; Wang, C. Existence of Solid Electrolyte Interphase in Mg Batteries: Mg/S Chemistry as an Example. *ACS Appl. Mater. Interfaces* **2018**, *10* (17), 14767–14776.
- (43) Meng, Z.; Foix, D.; Brun, N.; Dedryvère, R.; Stievano, L.; Morcrette, M.; Berthelot, R. Alloys to Replace Mg Anodes in Efficient and Practical Mg-Ion/Sulfur Batteries. *ACS Energy Lett.* **2019**, *4* (9), 2040–2044.
- (44) Richter, R.; Häcker, J.; Zhao-Karger, Z.; Danner, T.; Wagner, N.; Fichtner, M.; Friedrich, K. A.; Latz, A. Insights into Self-Discharge of Lithium– and Magnesium–Sulfur Batteries. *ACS Appl. Energy Mater.* **2020**, *3* (9), 8457–8474.
- (45) Xu, Y.; Ye, Y.; Zhao, S.; Feng, J.; Li, J.; Chen, H.; Yang, A.; Shi, F.; Jia, L.; Wu, Y.; Yu, X.; Glans-Suzuki, P. A.; Cui, Y.; Guo, J.; Zhang, Y. In Situ X-ray Absorption Spectroscopic Investigation of the Capacity Degradation Mechanism in Mg/S Batteries. *Nano Lett.* **2019**, *19* (5), 2928–2934.
- (46) Gao, T.; Hou, S.; Wang, F.; Ma, Z.; Li, X.; Xu, K.; Wang, C. Reversible S⁰/MgS_x Redox Chemistry in a MgTFSI₂/MgCl₂/DME Electrolyte for Rechargeable Mg/S Batteries. *Angew. Chem., Int. Ed.* **2017**, *56* (43), 13526–13530.
- (47) Yu, X.; Manthiram, A. Performance Enhancement and Mechanistic Studies of Magnesium–Sulfur Cells with an Advanced Cathode Structure. *ACS Energy Lett.* **2016**, *1* (2), 431–437.
- (48) Zhao-Karger, Z.; Bardaji, M. E. G.; Fuhr, O.; Fichtner, M. A new class of non-corrosive, highly efficient electrolytes for rechargeable magnesium batteries. *J. Mater. Chem. A* **2017**, *5* (22), 10815–10820.
- (49) Zhao-Karger, Z.; Liu, R.; Dai, W.; Li, Z.; Diemant, T.; Vinayan, B. P.; Minella, C. B.; Yu, X.; Manthiram, A.; Behm, R. J.; Ruben, M.; Fichtner, M. Toward Highly Reversible Magnesium–Sulfur Batteries with Efficient and Practical Mg[B(hfip)₄]₂ Electrolyte. *ACS Energy Lett.* **2018**, *3* (8), 2005–2013.
- (50) Li, X.; Gao, T.; Han, F.; Ma, Z.; Fan, X.; Hou, S.; Eidson, N.; Li, W.; Wang, C. Reducing Mg Anode Overpotential via Ion Conductive Surface Layer Formation by Iodine Additive. *Adv. Energy Mater.* **2018**, *8* (7), No. 1701728.
- (51) Vinayan, B. P.; Euchner, H.; Zhao-Karger, Z.; Cambaz, M. A.; Li, Z.; Diemant, T.; Behm, R. J.; Gross, A.; Fichtner, M. Insights into the electrochemical processes of rechargeable magnesium–sulfur batteries with a new cathode design. *J. Mater. Chem. A* **2019**, *7* (44), 25490–25502.
- (52) Kaland, H.; Fagerli, F. H.; Hadler-Jacobsen, J.; Zhao-Karger, Z.; Fichtner, M.; Wiik, K.; Wagner, N. P. Performance Study of MXene/Carbon Nanotube Composites for Current Collector- and Binder-Free Mg–S Batteries. *ChemSusChem* **2021**, *14* (8), 1864–1873.
- (53) Drews, J.; Jankowski, P.; Häcker, J.; Li, Z.; Danner, T.; Lastra, J. M. G.; Vegge, T.; Wagner, N.; Friedrich, K. A.; Zhao-Karger, Z.; Fichtner, M.; Latz, A. Modeling of Electron-Transfer Kinetics in

Magnesium Electrolytes: Influence of the Solvent on the Battery Performance. *ChemSusChem* **2021**, *14* (21), 4820–4835.

(54) Wang, L.; Diemant, T.; Li, Z.; Dasari, B.; Zhao-Karger, Z. Insights into the Degradation Mechanism of the Magnesium Anode in Magnesium–Chalcogen Batteries: Revealing Principles for Anode Design with a 3D-Structured Magnesium Anode. *ACS Appl. Energy Mater.* **2023**, *6* (2), 1008–1018.

(55) te Velde, G.; Bickelhaupt, F. M.; Baerends, E. J.; Fonseca Guerra, C.; van Gisbergen, S. J. A.; Snijders, J. G.; Ziegler, T. Chemistry with ADF. *J. Comput. Chem.* **2001**, *22* (9), 931–967.

(56) Pye, C. C.; Ziegler, T. An implementation of the conductor-like screening model of solvation within the Amsterdam density functional package. *Theor. Chem. Acc.* **1999**, *101* (6), 396–408.